

# Frequency-Domain Electromagnetic Induction Sensor Data Feature Extraction and Processing for Improved Landmine Detection

Stacy L. Tantum, Kenneth D. Morton, Jr., Leslie M. Collins, and Peter A. Torrione

Department of Electrical and Computer Engineering, Duke University  
Box 90291, Durham, NC 27708-0291

## ABSTRACT

Frequency-domain electromagnetic induction (EMI) sensors have the ability to provide target signatures which enable discrimination of landmines from harmless clutter. In particular, frequency-domain EMI sensors are well-suited for target characterization by inverting a physics-based signal model. In many model-based signal processing paradigms, the target signatures can be decomposed into a weighted sum of parameterized basis functions, where the basis functions are intrinsic to the target under consideration and the associated weights are a function of the target sensor orientation. The basis function parameters can then be used as features for classification of the target as landmine or clutter. In this work, frequency-domain EMI sensor data feature extraction and processing is investigated, with a variety of physics-based models and statistical classifiers considered. Results for data measured with a prototype frequency-domain EMI sensor at a standardized test site are presented. Preliminary results indicate that extracting physics-based features followed by statistical classification provides an effective approach for classifying targets as landmine or clutter.

**Keywords:** Landmine detection, RVM regression, statistical classification

## 1. INTRODUCTION

Electromagnetic induction (EMI) is one of several sensing modalities commonly employed for landmine detection. EMI sensors operate by inducing eddy currents in conducting bodies within the transmitted electromagnetic field, and then sensing the secondary field radiated from those bodies when the transmitter is turned off. Most EMI sensors can readily detect most mines, but they also detect most pieces of metallic debris, or clutter, and classifying the detected targets as either landmines or clutter is the primary challenge, particularly for mine types with lower metal content. The ability to distinguish between mines and clutter is critical, because not doing so results in unacceptably high false alarm rates.

Advanced signal processing algorithms for landmine detection using EMI sensor data often depend on an underlying parameterized signal model, where the model parameters are estimated and then used as features for landmine detection and/or classification.<sup>1-5</sup> Ideally, the number of features required is relatively small and the features themselves should be fairly stable and consistent for a given target type. Many times, the signal model takes the form of a weighted sum of parameterized basis functions, where the basis function parameters constitute the features utilized for subsequent classification.

One parameterized signal model that has been proposed for EMI sensor data is the discrete spectrum of relaxation frequencies (DSRF).<sup>5,6</sup> This model expresses the sensor response to a metallic target as a sum of terms, each characterized by a discrete relaxation frequency, and has been shown to provide a means of subsurface target classification for both landmine and unexploded ordnance detection.<sup>5-8</sup> A potential challenge associated with a model-based approach such as this is determining the correct model order, as the number of basis functions intrinsic to the target under consideration may not be known *a priori*.

A robust approach to estimating the DSRF from the measured sensor data without assuming prior knowledge of the model order is presented in,<sup>5</sup> in which basis pursuit is employed to cast the problem as an overdetermined set of linear equations. In that work, the goal was to estimate a physically meaningful target model, so physically relevant constraints were placed on the estimation such as constraining the weights on the DSRF components to be non-negative. In this

---

Further author information: (Send correspondence to L.M.C.)

S.L.T.: E-mail: stacy.tantum@duke.edu

P.A.T.: E-mail: peter.torrione@duke.edu

K.D.M.: Email: kenneth.morton@duke.edu

L.M.C.: E-mail: lcollins@ee.duke.edu, Telephone: 919-660-6260

Detection and Sensing of Mines, Explosive Objects, and Obscured Targets XVI,  
edited by Russell S. Harmon, John H. Holloway Jr., J. Thomas Broach, Proc. of SPIE  
Vol. 8017, 80170B · © 2011 SPIE · CCC code: 0277-786X/11/\$18 · doi: 10.1117/12.884769

Proc. of SPIE Vol. 8017 80170B-1

work, relevance vector machine (RVM) regression is applied to simultaneously determine both the parameterized basis functions in the DSRF and their relative contributions to the measured signal. In contrast to,<sup>5</sup> the goal in this work is to obtain consistent sparse target representations that may form the basis for subsequent target classification. As such, the sparse representations sought here are inspired by the sensor phenomenology but are not fully constrained by it, so the DSRF component weights found via RVM regression may be negative. However, as the goal of this work is to find sparse representations that are consistent across targets, this deviation from the underlying physics does not adversely affect achieving the goal. After obtaining a sparse target representation via RVM regression model inversion, a statistical classifier is then applied to the estimated parameters to classify the target as either landmine or clutter, as well as to identify the landmine type.

The remainder of this paper is organized as follows. The frequency-domain electromagnetic sensor with which data were collected and the associated data model are presented in Sec. 2, followed by a description of how RVM regression may be applied to obtain sparse target model representations in Sec. 3. Sec. 4 presents the algorithms developed and utilized for target detection and identification using sparse target model representations. Simulation and field data results then follow in Secs. 5 and 6, respectively. Finally, conclusions are presented in Sec. 7.

## 2. FREQUENCY-DOMAIN EMI SENSOR DESCRIPTION AND DATA MODEL

The EMI sensor considered in this work is a broadband frequency-domain sensor.<sup>9</sup> This sensor employs a dipole transmit coil and an array of three quadrupole receive coils arranged so that the sensor measures three responses in the cross-track direction as it moves forward (in the down-track direction). The response is measured at 21 logarithmically-spaced frequencies from 330 Hz to 90.03 kHz with a down-track sampling rate of 0.1 s, which corresponds to a spatial sampling interval of approximately 1 cm.<sup>10</sup> The quadrupole receive coil design produces a weak, minimal response when the receive coil is directly over a target due to the response in each half of the quadrupole being approximately equal, but of opposite polarity. To produce data with a peak over a target, the measured data are pre-processed by filtering in the down-track direction with the filter described in.<sup>9</sup> In addition to locating a peak response directly over a target, the filtering also mitigates sensor drift, improves the signal-to-noise ratio (SNR), and reduces the response due to the ground.<sup>9</sup>

The frequency-domain EMI sensor response to a metallic target can be expressed as a sum of the response terms, each characterized by a discrete relaxation,<sup>5,6</sup>

$$H(\omega) = c_0 + \sum_{k=1}^K \frac{c_k}{1 + j\omega/\zeta_k}, \quad (1)$$

where  $c_0$  represents an offset in the frequency response,  $c_k$  represents the real spectral amplitudes, and  $\zeta_k$  represents the relaxation frequencies. This representation is termed a discrete spectrum of relaxation frequencies (DSRF),<sup>5</sup> where each parameter pair  $(c_k, \zeta_k)$  corresponds to a single relaxation. The spectral amplitudes,  $c_k$ , are a function of the target's orientation and position with respect to the sensor, and so vary with the sensor's position over the target. The relaxation frequencies,  $\zeta_k$ , however, are intrinsic to the target, and therefore are invariant to the target's orientation and position with respect to the sensor. This invariance property renders the relaxation frequencies potentially powerful features for classifying and identifying interrogated targets.<sup>6</sup>

## 3. RVM REGRESSION FOR SPARSE MODEL REPRESENTATION

RVM regression is a technique which may be utilized to achieve a sparse representation of a signal.<sup>11,12</sup> Sparsity is achieved by decomposing the signal into a sum of weighted basis functions, or kernels, and determining the weights associated with the kernels such that the majority of the weights are zero. Thus, a few kernels possessing non-zero weights form the sparse representation of the signal. Generally, the kernel functions are determined prior to performing the regression, though they are typically chosen so they are effective for the problem at hand.

### 3.1 RVM Regression

Following the notation in Ref. 12, the signal is represented by

$$t = y(\mathbf{x}) + \mathbf{n} = \sum_{i=1}^M w_i \phi_i(\mathbf{x}) + \mathcal{N}(\mathbf{n}|0, \beta^{-1}), \quad (2)$$

where  $t$  represents the target variable (the measured data),  $\mathbf{x}$  represents the independent variables (the sample times for the data),  $\phi_i$  represents the  $i^{th}$  basis function, or kernel,  $w_i$  represents the weight associated with the  $i^{th}$  kernel, and  $\mathbf{n}$  represents Gaussian noise with mean 0 and precision  $\beta^{-1}$ , or variance  $\beta = \sigma^2$ . Thus, the measured data are distributed according to<sup>12</sup>

$$p(t|\mathbf{x}, \mathbf{w}, \beta) = \mathcal{N}(t|y(\mathbf{x}), \beta^{-1}). \quad (3)$$

In standard RVM regression, a kernel is associated with every data point in the training set, and a common choice for the kernels are radial basis functions (RBFs). Assuming there are  $N$  observations, the likelihood of the entire set of target values,  $\mathbf{t} = (t_1, \dots, t_N)^T$  is<sup>12</sup>

$$p(\mathbf{t}|\mathbf{X}, \mathbf{w}, \beta) = \prod_{n=1}^N p(t_n|\mathbf{x}_n, \mathbf{w}, \beta^{-1}), \quad (4)$$

where  $\mathbf{X}$  contains all of the measured data, with row  $n$  corresponding to the  $n^{th}$  measurement. Sparsity in the weights,  $\mathbf{w}$ , is achieved by assuming a zero-mean Gaussian prior on the weights, where the prior for each weight has its own precision hyperparameter,  $\alpha_i$ . Under these assumptions, the prior on the weight vector is<sup>12</sup>

$$p(\mathbf{w}|\alpha) = \prod_{i=1}^M \mathcal{N}(w_i|0, \alpha_i^{-1}), \quad (5)$$

and the posterior distribution for the weights is a Gaussian of the form<sup>12</sup>

$$p(\mathbf{w}|\mathbf{t}, \mathbf{X}, \alpha, \beta) = \mathcal{N}(\mathbf{w}|\mathbf{m}, \Sigma), \quad (6)$$

with  $\mathbf{m} = \beta \Sigma \Phi^T \mathbf{t}$ ,  $\Sigma = (\mathbf{A} + \beta \Phi^T \Phi)^{-1}$ , and  $\mathbf{A} = \text{diag}(\alpha_i)$ . The hyperparameters,  $\alpha_i$  and  $\beta$ , are determined by maximizing the evidence,  $p(\mathbf{t}|\mathbf{X}, \alpha, \beta)$ , with respect to the hyperparameters. After performing this optimization, the majority of the hyperparameters,  $\alpha_i$ , go to infinity, which corresponds to the variance of the distributions for a majority of the weights going to zero. Thus, the majority of the weights,  $w_i$ , go to zero, leaving only a small subset of the kernels to represent the signal.

### 3.2 RVM Regression for Model Inversion

RVM regression is typically applied to retain a small number of relevant vectors from the training data which then form the basis for a sparse model based on the chosen kernel function. RVM regression may also be applied to select a small number of parametric model-based kernel functions to form a sparse model-based representation for the measured data. For the DSRF signal model considered here, RVM regression is applied to simultaneously estimate the model order and the relaxations,  $(c_k, \zeta_k)$ , for measured frequency-domain EMI data, assuming the signal model in Eq. (1). In this case, the kernel function is chosen to be the portion of the signal model [Eq. (1)] corresponding to the relaxation frequency,

$$\phi_i(\omega) = \frac{1}{1 + j\omega/\zeta_i}, \quad (7)$$

and the weights determined by the RVM regression correspond to the real spectral amplitudes,  $c_i$ . The kernel functions are calculated over the range of frequencies measured by the sensor, 330 Hz to 90.03 kHz, and the parameters of the kernel functions,  $\zeta_i$ , are selected so they are logarithmically spaced from 30 Hz to 900 kHz, which corresponds to approximately one decade above and below the sensor bandwidth.

## 4. TARGET DETECTION AND IDENTIFICATION USING SPARSE MODELS

While RVM regression will determine a sparse set of relevant kernels, there are no constraints forcing the relevant kernels (relaxation frequencies in this application) to be non-adjacent. In some instances, the RVM regression results in two or more adjacent relaxation frequencies being deemed relevant. This typically indicates that the true relaxation frequency lies between the two adjacent relaxation frequencies used to build the dictionary. Prior to utilizing the estimated relaxation frequencies for target identification or detection, it may be beneficial to coalesce adjacent relaxation frequencies into a single relaxation frequency. An example of this situation is the estimated DSRF for Example #3 of LMAP #8, shown in the bottom-left panel in Fig. 7. In this example, the two relaxation frequencies of approximately  $\log_{10} \zeta_i = 4.8$  Hz,

are coalesced into a single relaxation frequency by interpolating between the adjacent relaxation frequencies using the relationships given in.<sup>5</sup> The interpolated relaxation frequency is given by<sup>5</sup>

$$\log_{10}(\zeta_{intp}) = \log_{10}(\zeta_a) + \frac{c_b}{c_a + c_b} \log_{10}(\zeta_b/\zeta_a), \quad (8)$$

and the interpolated real spectral amplitude is given by<sup>5</sup>

$$c_{intp} = c_a + c_b. \quad (9)$$

The above relationships are appropriate when only two adjacent relaxation frequencies have non-zero magnitude. In our work, however, RVM regression can produce estimated DSRFs with three or more adjacent relaxation frequencies with non-zero magnitude, particularly in low SNR scenarios. To address these situations, the above relationships have been extended so that a single relaxation frequency estimate may be interpolated from more than two relaxation frequencies. In this case, the interpolated relaxation frequency is given by

$$\log_{10}(\zeta_{intp}) = \log_{10}(\zeta_{MAX_c}) + \sum_{\substack{m=1 \\ m \neq MAX_c}}^M \frac{c_m}{c_{MAX_c} + c_m} \log_{10} \left( \frac{\zeta_m}{\zeta_{MAX_c}} \right), \quad (10)$$

where  $MAX_c$  denotes the relaxation frequency with the largest spectral amplitude, and the interpolated real spectral amplitude is given by

$$c_{intp} = \sum_{m=1}^M c_m. \quad (11)$$

The following sections describe how the distance between two targets described by the DSRF model may be assessed, as well as distance-based and Bayesian approaches to identification, classification, and detection.

#### 4.1 Earth Mover's Distance

Earth Mover's Distance (EMD) was first proposed as a measure of the distance between two feature distributions within the context of image analysis.<sup>13</sup> Although EMD was originally proposed to measure the distance between two distributions, it can also be applied to measure the distances between two spectra.<sup>5</sup> A physical analogy is to view the first spectrum as piles of earth with mass and spatial distribution according to the first spectrum, and the second spectrum as holes in the ground also distributed spatially according to that spectrum and with volumes needed to accommodate the mass of earth proportional to the spectral magnitude.<sup>13</sup> Continuing the analogy, the EMD measures the minimum amount of work required to move the mass (piles of earth) in the first spectrum to fill the holes in the second spectrum, where work is the product of mass and distance. The solution to this linear programming problem is outlined in Ref. 13, and its application to measuring the similarity between DSRFs is presented in Ref. 5.

#### 4.2 Distance-Based Classifiers

Distance-based classifiers generally consider the distance of the data under test to the training data, and classify the test data according to the  $K$  most similar training data points, where  $K$  is a parameter that must be selected. Although Euclidean distance is a typical choice for measuring the similarity between the training data and the test data, there are many other distance measures that may be utilized. In this work, the estimated DSRFs, each of which is succinctly characterized by a set of  $F$  coalesced relaxations  $(c_f, \zeta_f)$ , form the data to which the classifier is applied, and EMD is utilized to measure the distance between the estimated DSRFs. Since EMD was originally defined for distributions, it assumes the two vectors under comparison have components with non-negative weights. The application of RVM regression considered here does not constrain the component weights to be non-negative, however, so the EMD is determined using the magnitude of the real spectral amplitudes.

### 4.2.1 K-Nearest Neighbor

The K-Nearest Neighbor (KNN) classifier considers the  $K$  training points most similar to the test data, and classifies the test data according to the majority class of those  $K$  nearest training data points. Mathematically, the decision statistic for a binary decision KNN classifier may be expressed as<sup>14</sup>

$$\kappa(x) = \frac{k_{H_1}}{K}, \quad (12)$$

where  $K$  is the number of nearest-neighbors considered for the classification decision and  $k_{H_1}$  is the number of the  $K$  nearest neighbor training points associated with hypothesis  $H_1$ . In this application, the nearest neighbors are determined using EMD is to measure the distance between the test point and the training points.

### 4.2.2 Distance Likelihood Ratio Test

The distance likelihood ratio test (DLRT) is an approximation to the likelihood ratio test with the required probability density functions estimated via KNN density estimation, and is given by.<sup>15</sup>

$$\hat{\lambda}(x) = \log \left( \frac{n_{H_0}}{n_{H_1}} \right) + D [\log (\Delta_{K^{(0)}}) - \log (\Delta_{K^{(1)}})], \quad (13)$$

where  $n_{H_i}$  is the number of training points associated with hypothesis  $H_i$ ,  $D$  is the dimensionality of the feature space, and  $\Delta_{K^{(i)}}$  is the distance to the  $k^{th}$  neighbor from hypothesis  $H_i$ . Here, the distance  $\Delta$  is measured using EMD. In this application, the dimensionality of the feature space is equal to the number of kernels in the RVM regression model inversion. In practice, a monotonic function of the DLRT,

$$\hat{\lambda}'(x) = \log (\Delta_{K^{(0)}}) - \log (\Delta_{K^{(1)}}), \quad (14)$$

is used to calculate the decision statistic for this classifier.

### 4.3 Bayesian Target Identification and Detection

A Bayesian approach to target identification and detection is also considered. Assuming the data vector  $\mathbf{x} = [x_1 x_2 \cdots x_F]$  contains the  $F$  coalesced relaxation frequencies,  $\zeta_f$ , determined to be relevant by the RVM regression model inversion,  $\mathbf{x}$ , the *a posteriori* probability of a particular mine type  $t_m$  given the data  $\mathbf{x}$  is given by

$$f(t_m|\mathbf{x}) = \frac{f(\mathbf{x}|t_m)f(t_m)}{f(\mathbf{x})}, \quad (15)$$

which reduces to

$$f(t_m|\mathbf{x}) = \frac{\prod_{f=1}^F f(x_f|t_m)f(t_m)}{f(\mathbf{x})} \quad (16)$$

with the simplifying assumption that all the coalesced relaxation frequencies in  $\mathbf{x}$  are independent. Further assuming that  $f(\mathbf{x})$  and  $f(t_m)$  are constant, this expression reduces to

$$f(t_m|\mathbf{x}) \propto \prod_{f=1}^F f(x_f|t_m), \quad (17)$$

which forms the basis for determining the maximum likelihood estimate of the target by choosing the target  $m$  for which (17) is maximum. The required probability density functions (pdfs) are found via kernel density estimation.<sup>14</sup>

A similar approach to that taken for mine target identification is taken for detection of mines from blanks and/or clutter. The likelihood ratio is given by

$$\lambda(\mathbf{x}) = \frac{f(\mathbf{x}|H_1)}{f(\mathbf{x}|H_0)} = \frac{\sum_{m=1}^M f(\mathbf{x}|t_m, H_1)f(t_m)}{f(\mathbf{x}|H_0)}. \quad (18)$$

Table 1. Model parameters for the synthetic four-relaxation target, from which synthetic data is generated using the DSRF model [Eq. (1)].

Term (k)	Relaxation Frequency [Hz] ( $\zeta_k$ )	Spectral Amplitude ( $c_k$ )
1	1400	0.25
2	1620	0.25
3	18350	0.25
4	207980	0.25

Again, assuming  $f(\mathbf{x}|\mathbf{H}_0)$  and  $f(t_m)$  are constant,

$$\lambda(\mathbf{x}) \propto \sum_{m=1}^M \left[ \prod_{f=1}^F f(x_f|t_m, \mathbf{H}_1) \right], \quad (19)$$

and the required pdfs are found via kernel density estimation.<sup>14</sup>

## 5. DSRF ESTIMATION SIMULATION RESULTS

The efficacy of the proposed model inversion technique using RVM regression is first evaluated through a simulation study. To facilitate comparison of performance trends to previously proposed DSRF model estimation techniques, the simulation study presented here is modeled after the four-relaxation DSRF simulation study presented in.<sup>5</sup>

In practice, it may be difficult, if not impossible, to analytically derive the DSRF for a real-world target (i.e., a landmine). In these instances, a reasonable approach may be to take careful measurements of representative examples of a target to experimentally determine a DSRF model. To simulate this process, the DSRF is estimated from noise-free synthetic data to determine the noise-free DSRF. The noise-free DSRF becomes the standard to which estimated DSRFs are compared in order to evaluate performance under realistic conditions. Performance is assessed by evaluating the EMD between the estimated DSRF and the true DSRF, as well as between the estimated DSRF and the noise-free DSRF. The first performance measure indicates how well the model inversion can identify the true underlying target model. The second performance measure considers how well the model inversion may perform in a realistic scenario, where the true underlying target model may not be known and must be estimated.

The simulated data for a synthetic four-relaxation target is generated according to (1) using the relaxation frequencies and spectral amplitudes given in Table 1, and corrupted by zero-mean white Gaussian noise with standard deviation  $\sigma_n^2$ . The signal-to-noise ratio (SNR), defined in decibels as

$$\text{SNR}_{\text{dB}} = 10 \log_{10} \frac{1}{\sigma_n^2} \sum_i |H(\omega_i)|^2, \quad (20)$$

ranges from 20 dB to 90 dB. Additionally, there are 225 kernels in the dictionary, about twice the 25 per decade suggested in Ref. 5 (App. B). The selection of the discretization of the relaxation frequency for the kernel function was determined by examining the estimated relaxation frequencies in a noise-free scenario as a function of the number of kernel functions, shown in Fig. 1. The estimated DSRFs are shown by the dots, and the relaxation frequencies of the true DSRF are provided by the dashed lines for reference. The noise-free DSRF estimates converge and become fairly stable when the number of model inversion kernels is greater than about 200. Increasing the number of kernels beyond 200 does not significantly improve the relaxation frequency estimates, but does lead to greater computational burden, as the time required perform the RVM regression increases significantly with the number of kernels. This choice of discretization for the relaxation frequencies, about 50 per decade, is anticipated to provide adequate resolution without unnecessarily increasing the computational burden.

It is interesting to note that even with a very large number of kernels (although not shown here, up to 2000 were considered in this investigation), the RVM regression is unable to resolve the two lowest relaxation frequencies. The

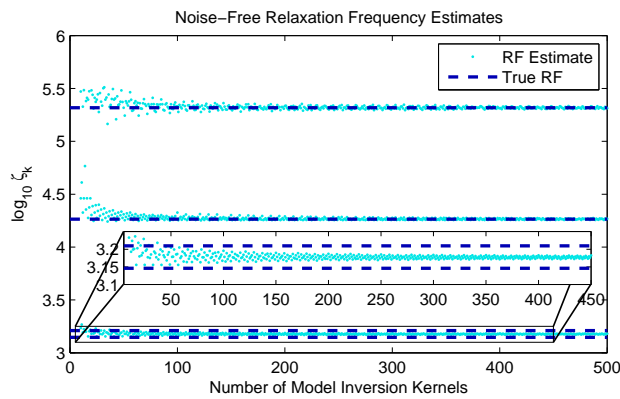


Figure 1. Estimated relaxation frequencies for the four-relaxation example (noise-free data) as a function of the number of model inversion kernels.

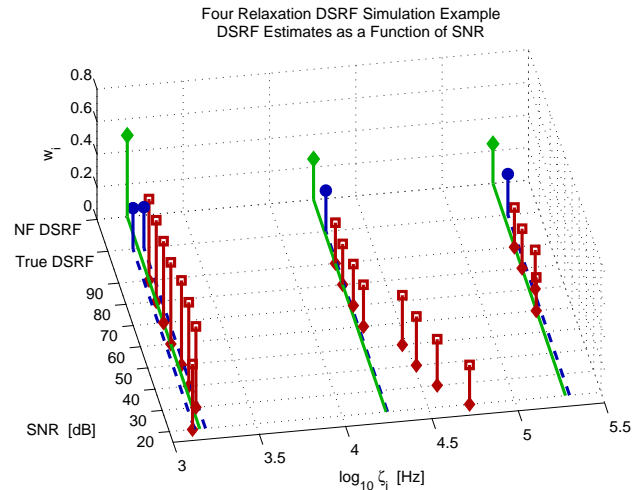


Figure 2. Example estimated DSRFs for the four-relaxation synthetic example as a function of SNR. The true DSRF is shown by the filled circles and dashed lines, and the noise-free (NF) DSRF estimate is shown by the filled diamonds and solid lines.

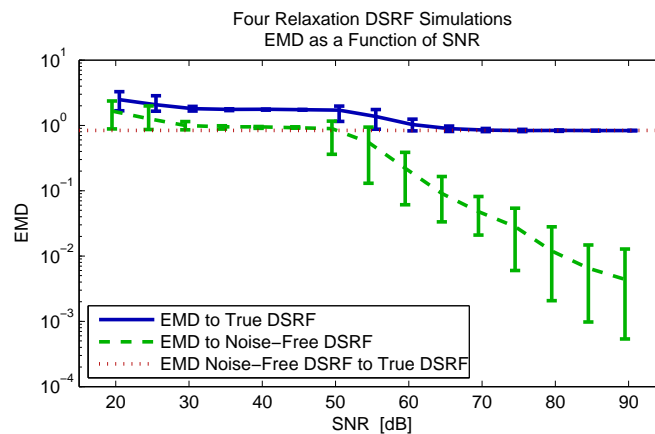


Figure 3. Mean EMD as a function of SNR for the four-relaxation synthetic example. Error bars represent the 10<sup>th</sup> and 90<sup>th</sup> percentiles.

inset in Fig. 1 clearly shows that the solution converges to a single estimated relaxation frequency between the two lowest relaxation frequencies. As a consequence, the EMD between the true DSRF for this example and the noise-free estimates never reaches zero. Since the RVM regression model inversion seeks a sparse representation, the solution with a single relaxation between the two lowest relaxations is preferred to the solution that includes those two relaxations.

A set of example DSRF estimates is shown in Fig. 2, illustrating how they evolve with increasing SNR. The true DSRF is shown at the top of the plot with the filled circles, and dashed lines form reference points to which the DSRF estimates can be compared. The noise-free DSRF estimate is also shown at the top of the plot with filled diamonds, with solid lines as reference points. The DSRF estimates at each SNR are shown with the open squares, and can be compared to the dashed and solid lines from the true DSRF and noise-free DSRF estimate, respectively. In this example, RVM regression estimates two relaxation frequencies at SNRs up to 50 dB, and three relaxation frequencies at SNRs above 50 dB. As anticipated, the DSRF estimates converge to the noise-free DSRF estimate, but not to the true DSRF.

The mean EMD to the true DSRF and noise-free DSRF estimate are shown in Fig. 3 with error bars indicating the 10<sup>th</sup> and 90<sup>th</sup> percentiles. At each SNR, the DSRF was estimated for 1000 random realizations of the synthetic signal. The EMD to the true DSRF is shown by the solid line, and the EMD to the noise-free DSRF estimate is shown by the dashed

line. Slight horizontal offsets have been added to both curves to ensure the error bars are visually distinct. The EMD between the noise-free DSRF estimate and the true DSRF is also shown with the dotted line.

It is interesting to note that as SNR increases, the mean EMD to the true DSRF decreases, plateaus, and then decreases and plateaus again. The plateau effects are caused by the RVM regression determining that only two RFs are relevant at lower SNRs, and then determining that only three RFs are relevant for higher SNRs. For the plateau around 40 dB, the RVM regression model inversion is converging to the best solution it can determine with only two relaxation frequencies, as the data do not support including more relaxation frequencies due to the lower SNR. For the plateau above 80 dB, the estimated DSRF converges to the noise-free DSRF estimate, as the two lowest relaxation frequencies cannot be resolved. This is demonstrated by the EMD between the estimated DSRF and the true DSRF (solid line) converging to the EMD between the noise-free DSRF estimate and the true DSRF (dotted line). The plateau effect, however, is not seen at higher SNRs in the EMD to the noise-free DSRF estimate. Once the data support estimating three relaxation frequencies, the RVM regression provides DSRF estimates that continually approach the noise-free DSRF estimate. For this reason, the EMD to the noise-free DSRF estimate is much smaller than the EMD to the true DSRF at higher SNRs.

## 6. FIELD TEST RESULTS

Data were collected over an assortment of mine targets and emplaced clutter at a standardized test facility in a temperate climate. The test facility contains a variety of high-metal anti-personnel (HMAP) mines, low-metal anti-personnel (LMAP) mines, and low-metal anti-tank (LMAT) mines, as well as an array of clutter targets. Data were collected over each target in two opposing directions, and in this analysis the two collections are considered in aggregate. Although data are collected at a series of downtrack sensor positions over each target, only the single measurement with the maximal response after pre-processing<sup>9</sup> is selected for further processing.

The identification and classification algorithms presented here are trained and tested on the measured data using a Leave-One-Target-Out (LoTo) cross-validation procedure. In this procedure, the measured data for both passes over a given target example are reserved for testing, while all the remaining data is utilized for testing. Note that while a given target type example is reserved for testing, other examples of that target type are present in the training data. This process is repeated for each target example present in the test facility.

### 6.1 Sparse Target Model Representations

RVM regression model inversion is applied to estimate the DSRFs for the targets measured in the standardized test facility. Although the results presented in<sup>5</sup> retained the DC term ( $c_0$ ) in the DSRF signal model (1) when estimating the DSRF, that term was not utilized in subsequent processing. In this work, the DC term ( $c_0$ ) is not included in the model when the RVM regression is applied for model inversion; only the terms corresponding to the model-based kernels (7), which constitute the estimated DSRF, are utilized for the RVM regression as well as subsequent target identification or detection.

Example RVM regression model inversion results for a HMAP mine type are shown in Figs. 4 and 5, and similar results for a LMAP mine type follow in Figs. 6 and 7. In both cases, four examples of the specified mine type are presented. The Argand diagrams (Figs. 4 and 6) show the measured data as dots and the RVM regression model inversion as a solid line. Although the magnitude of the sensor response varies considerably for the different examples of the mine type, the general shape of the curve is consistent across the four examples of each mine type. The corresponding estimated DSRFs (Figs. 5 and 7) demonstrate that the sparse representations found via RVM regression model inversion are quite consistent despite the differences in the original data; the relaxation frequencies and the relative amplitudes of the real spectral components are nearly identical. The differences in the amplitudes of the real spectral components can be attributed to the differences in the magnitude of the original data.

### 6.2 Target Identification and Detection

The results of applying the Bayesian approach for mine target identification are shown in Fig. 8. This figure provides an identification confusion matrix and shows the probability of declaring a mine target type (response) given the true mine target type (truth). The number of targets of a particular type in the data set appears in brackets on the right-hand side of the matrix. The closer this matrix is to being diagonal (top-left to bottom-right) the better identification performance is achieved. As this figure shows, target identification performance is strong: overall performance is 71.4% correct identification, compared to 4.5% correct identification by chance. It is interesting to note that there is some block



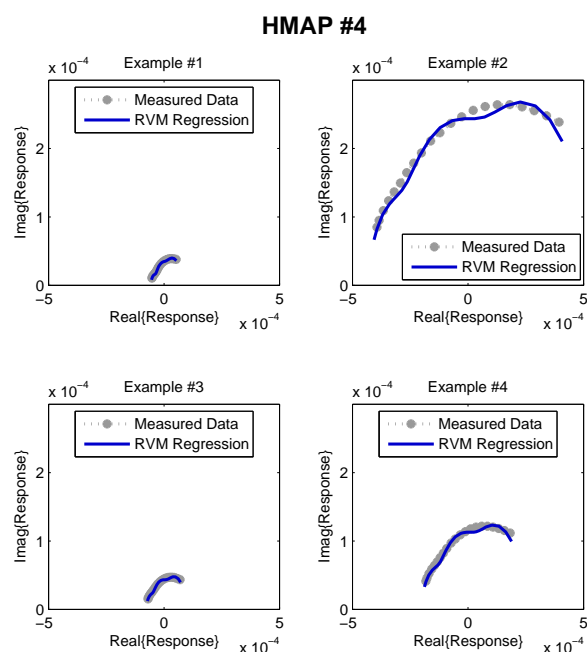


Figure 4. Argand diagrams for example RVM regression model inversion for mine type HMAP #4.

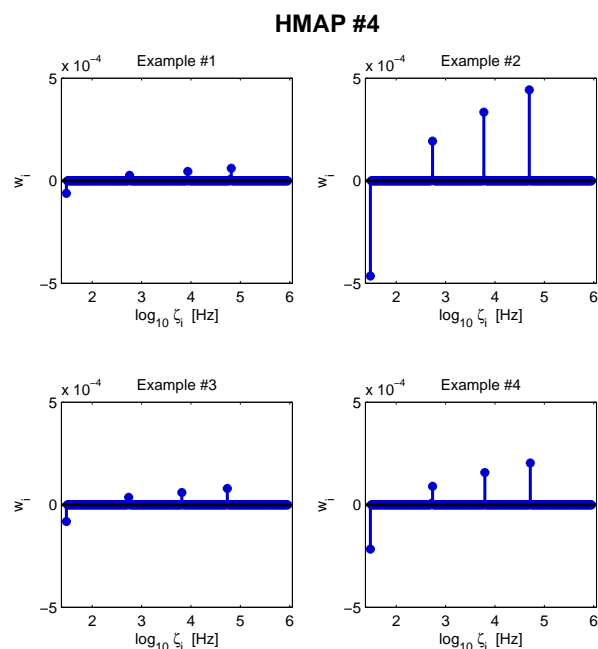


Figure 5. Estimated DSRFs for example RVM regression model inversion for mine type HMAP #4.

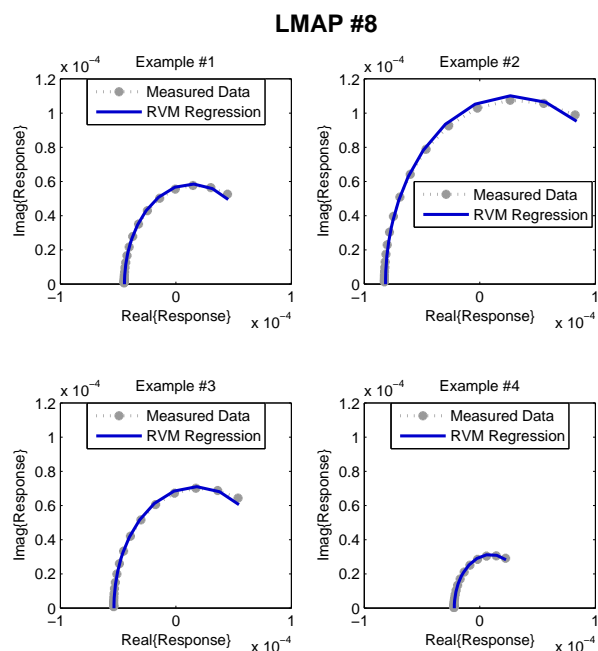


Figure 6. Argand diagrams for example RVM regression model inversion for mine type for LMAP #8.

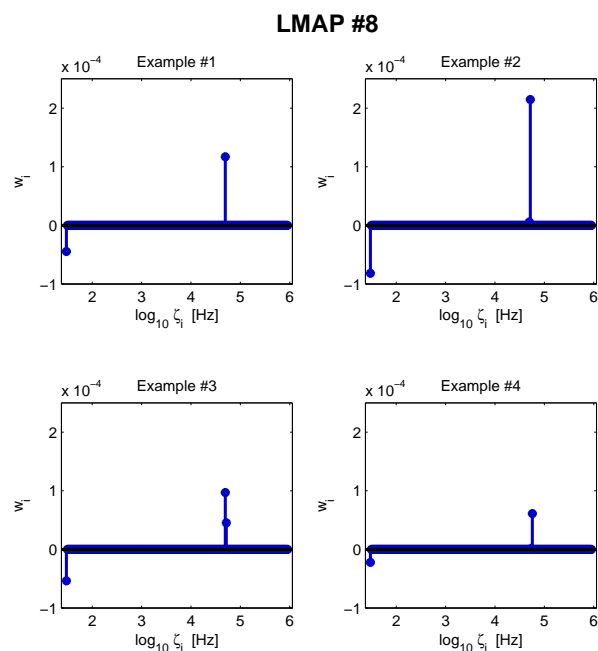


Figure 7. Estimated DSRFs for example RVM regression model inversion for mine type for LMAP #8.

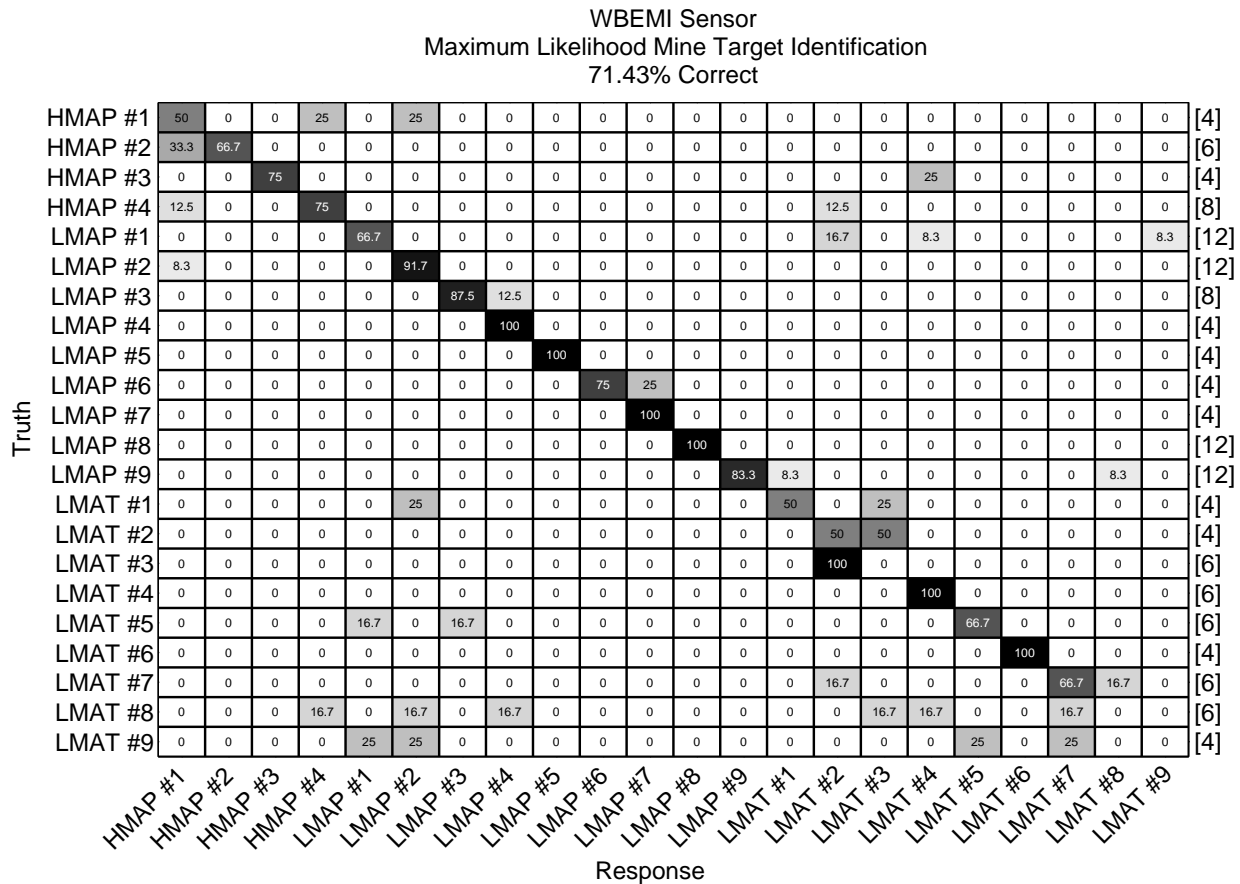


Figure 8. Bayesian maximum likelihood mine target type identification performance.

diagonal structure to the identification confusion, where many mines that are mis-identified are mistaken with a mine of the same class (HMAP, LMAP, or HMAP). A confusion matrix that considers if a mine is identified in the correct class (HMAP, LMAP, or HMAP), as opposed to the correct mine type, is presented in Fig. 9. This class confusion matrix confirms the trend suggested in the identification confusion matrix. The overall percent correct for mine class is 87.1%, which is substantially higher than percent correct by random chance of 33.3%.

Detection results obtained using the KNN and DLRT distance-based classifiers as well as the likelihood ratio decision statistic are shown in Fig. 10 and Fig. 11. The KNN classifier tends to have the strongest performance for landmine detection against both blanks and clutter (Fig. 10) and blanks alone (Fig. 11). The DLRT performance tends to follow the KNN performance at low  $P_{FA}$  and the Bayesian performance at high  $P_{FA}$ . The Bayesian approach tends to underperform both distance-based classifiers on this data set. This may be due to the distance-based classifiers (KNN and DLRT) taking into consideration both the relaxation frequencies and their associated real spectral amplitudes, while the Bayesian approach only considers the relaxation frequencies.

## 7. SUMMARY AND FUTURE WORK

Results obtained on data measured at a standardized test facility in a temperate climate indicate that RVM regression model inversion to find DSRF parameter estimates appears to provide sparse, stable representations of landmine targets using frequency-domain EMI sensor data. Landmines can be correctly identified and classified by type at a rate much better than chance, and detection performance is strong.

Future work entails investigating modifications to the RVM regression that would enable constraining the real spectral amplitudes to be non-negative, and hence forcing them to be consistent with the underlying phenomenology as well

WBEMI Sensor  
Mine Target Classification from ML ID  
87.14% Correct

Truth	HMAP	86.4	4.5	9.1	[22]
	LMAP	1.4	90.3	8.3	[72]
	LMAT	2.2	15.2	82.6	[46]
		HMAP	LMAP	LMAT	
		Response			

Figure 9. Mine target type classification performance from Bayesian maximum likelihood identification.

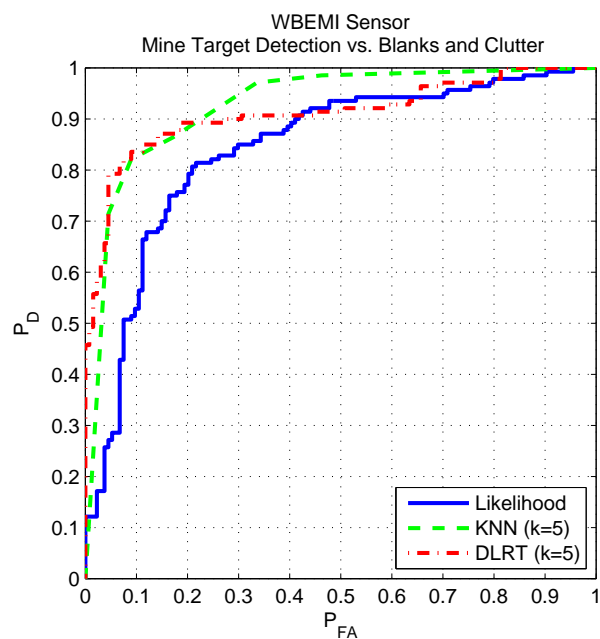


Figure 10. Mine target detection performance versus blanks and clutter.

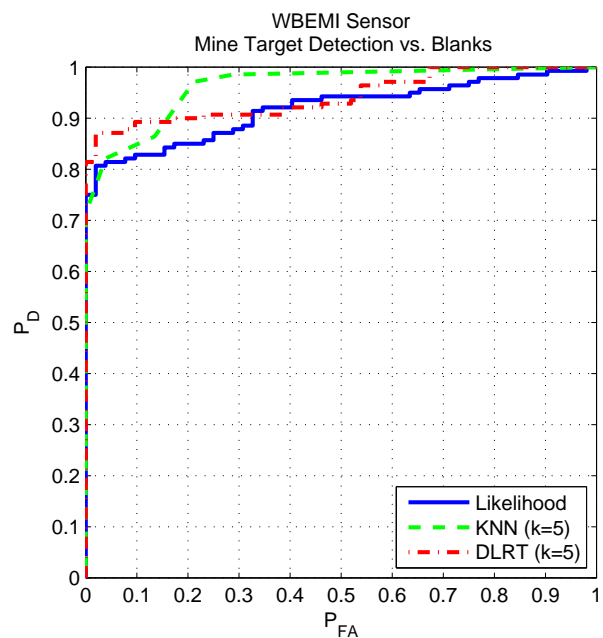


Figure 11. Mine target detection performance versus blanks only.

as improving the Bayesian classifier so that it jointly considers both the relaxation frequencies and their associated real spectral amplitudes. In addition, different mine types typically produce markedly different sensor response energies, so an appropriately designed energy-based pre-screener could further improve performance, as it has for other processing methods.<sup>16</sup>

## ACKNOWLEDGMENTS

This work is supported by the US Army RDECOM CERDEC Night Vision and Electronic Sensors Directorate (NVESD) and the Army Research Office (ARO).

## REFERENCES

1. L. M. Collins, P. Gao, and L. Carin, "An improved Bayesian decision theoretic approach for land mine detection," *IEEE Transactions on Geoscience and Remote Sensing* **37**(2), pp. 811–819, 1999.
2. P. Gao, L. M. Collins, P. Garber, N. Geng, and L. Carin, "Classification of landmine-like metal targets using wideband electromagnetic induction," *IEEE Transactions on Geoscience and Remote Sensing* **38**, pp. 1352–1361, May 2000.
3. S. L. Tantom and L. M. Collins, "A comparison of algorithms for subsurface target detection and identification using time domain electromagnetic data," *IEEE Transactions on Geoscience and Remote Sensing* **39**(6), pp. 1299–1306, 2001.
4. E. B. Fails, P. A. Torriane, W. R. Scott, Jr., and L. M. Collins, "Performance of a four parameter model for modeling landmine signatures in frequency domain wideband electromagnetic induction systems," in *Proceedings of SPIE: International Symposium on Aerospace/Defense Sensing, Simulation, and Controls*, **6553**, p. 65530D, 2007.
5. M.-H. Wei, W. R. Scott, Jr., and J. H. McClellan, "Robust estimation of the discrete spectrum of relaxations for electromagnetic induction responses," *IEEE Transactions on Geoscience and Remote Sensing* **48**, pp. 1169–1179, March 2010.
6. L. Carin, H. Yu, Y. Dalichaouch, and C. Baum, "On the wideband EMI response of a rotationally symmetric permeable and conducting target," *IEEE Transactions on Geoscience and Remote Sensing* **39**(6), pp. 1206–1213, 2001.
7. Y. Zhang, L. M. Collins, H. Yu, C. Baum, and L. Carin, "Sensing of unexploded ordnance with magnetometer and induction data: Theory and signal processing," *IEEE Transactions on Geoscience and Remote Sensing* **41**(5), pp. 1005–1015, 2003.
8. Y. Zhang, L. M. Collins, and L. Carin, "Unexploded ordnance detection using Bayesian physics-based data fusion," *Integrated Computer-Aided Engineering* **10**, pp. 231–247, 2003.
9. W. R. Scott, Jr., "Broadband array of electromagnetic induction sensors for detecting buried landmines," in *Proceedings of the IEEE International Geoscience and Remote Sensing Symposium, 2008*, **II**, pp. II–375 – II–378, July 2008.
10. A. C. Gurbuz, W. R. Scott, Jr., and J. H. McClellan, "Location estimation using a broadband electromagnetic induction array," in *Proceedings of SPIE: Detection and Sensing of Mines, Explosive Objects, and Obscured Targets XIV*, R. S. Harmon, J. T. Broach, and J. H. Holloway Jr., eds., **7303**, p. 73030U, 2009.
11. M. E. Tipping, "Sparse Bayesian learning and the relevance vector machine," *Journal of Machine Learning Research* **1**, pp. 211–244, June 2001.
12. C. M. Bishop, *Pattern Recognition and Machine Learning*, Springer Science, 2006.
13. Y. Rubner, C. Tomasi, and L. J. Guibas, "A metric for distributions with applications to image databases," in *Proceedings of the 1998 IEEE International Conference on Computer Vision*, (Bombay, India), 1998.
14. R. O. Duda, P. E. Hart, and D. G. Stork, *Pattern Classification*, John Wiley & Sons, Inc., 2001.
15. J. J. Remus, K. D. Morton, P. A. Torriane, S. L. Tantom, and L. M. Collins, "Comparison of a distance-based likelihood ratio test and k-nearest neighbor classification methods," in *Machine Learning for Signal Processing*, pp. 362–367, (Cancun, Mexico), 2008.
16. P. Torriane and L. Collins, "Performance comparison of automated induction-based algorithms for landmine detection in a blind field test," *Subsurface Sensing Technologies and Applications* **5**(3), pp. 121–150, 2004.